PdM nanoparticles (M = Ni, Co, Fe, Mn) with high activity and stability in formic acid oxidation synthesized by sonochemical reactions

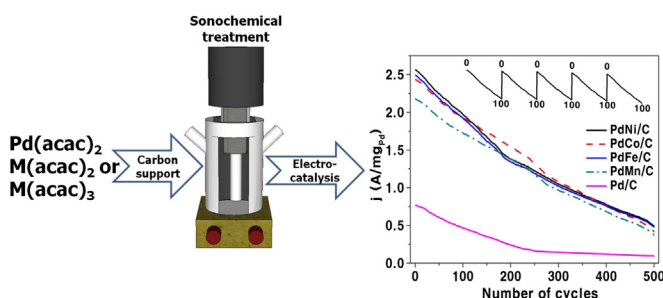Md. Abdul Matin [a], Ji-Hoon Jang [b], Young-Uk Kwon [a,b],*

[a] Department of Chemistry, Sungkyunkwan University, Suwon 440-746, Republic of Korea
[b] Center for Human Interface Nano Technology, Sungkyunkwan University, Suwon 440-746, Republic of Korea

HIGHLIGHTS

- We synthesize alloy nanoparticles with Pd and M (M = Ni, Co, Fe, Mn) whose their composition is 1:1.
- The ultrasound-assisted polyol method is used to synthesize alloy nanoparticles.
- The analysis data prove the alloy structure of the nanoparticles.
- PdM alloys show 2–3.5 times higher current density in catalytic activity than pure Pd.

GRAPHICAL ABSTRACT

ARTICLE INFO

ABSTRACT

Bimetallic alloy Pd_nM ($n = 1$ for M = Mn, Fe, and Co; $n = 1$, 2, and 3 for M = Ni) nanoparticles (NPs) are synthesized on carbon supports by sonochemical reactions of $Pd(acac)_2$ (acac = acetylacetonate) with $M(acac)_2$ (M = Ni, Co, Mn) or $Fe(acac)_3$ in ethylene glycol. The NPs are characterized by powder X-ray diffractometry, transmission electron microscopy (TEM), and inductively coupled plasma-atomic emission spectroscopy to determine their crystal structures, particle sizes, morphology, and elemental compositions. Alloy formation of the NPs is proven by energy dispersive X-ray spectroscopy line profiles using scanning TEM. The electronic structures and the surface compositions of NPs are analyzed using X-ray photoelectron spectroscopy, and Fourier-transform infrared spectroscopy, respectively. Pd_nM NPs are applied as electrocatalysts for formic acid oxidation. The incorporation of M in Pd reduces the poisoning by surface hydroxyl groups. Activities based on the current densities are in the order of PdNi > PdFe > PdCo > PdMn. Within the Pd_nNi series, the activity is in the order of PdNi > Pd_2Ni > Pd_3Ni. The Pd_nM NP electrocatalysts show higher activity by a factor of 2–3.5 and improved durability than similarly prepared Pd NP electrocatalyst.

1. Introduction

The increasing worldwide energy demand and environment concerns have stimulated extensive research into power sources with high energy conversion efficiency and low pollutant emissions [1]. Fuel cell technology is one of the most studied fields in this regard due to its unique properties, which include relatively clean exhaust and high energy density. Among the various types of fuel cells, proton exchange membrane fuel cells, direct methanol fuel cells, and direct formic acid fuel cells (DFAFCs) are suggested to be the most competitive choices for automobile and portable electronic applications [2–4].

* Corresponding author. Department of Chemistry, Sungkyunkwan University, Suwon 440-746, Republic of Korea. Tel.: +82 31 290 7070; fax: +82 31 290 7075.
E-mail address: ywkwon@skku.edu (Y.-U. Kwon).

Recently, much attention has been focused on DFAFCs because formic acid has a lower oxidation potential, better oxidation kinetics, and a lower crossover rate than methanol due to the repulsive interactions between the Nafion membrane and formate anions [5,6]. Although notable progress in DFAFCs has been achieved, several issues have precluded their use in real applications [7]. Further, no catalysts reported thus far satisfy all of the requirements of performance, stability, and availability for real applications [8]. For instance, Pt catalyst is seriously poisoned by CO, which is formed as a reaction intermediate during the indirect dehydration pathway of the formic acid oxidation (FAO) reaction [8,9]. Even if this CO poisoning problem can be solved, the high cost and scarcity of Pt [10–13] are expected to be serious challenges for Pt-based electrocatalysts. On the other hand, electrocatalysis by Pd catalysts occurs through the direct dehydrogenation pathway, which is less susceptible to the CO poisoning effect, exhibiting high initial activity. For these reasons, Pd catalysts are gaining increasing importance as electrocatalysts for DFAFCs. Pd catalysts, however, suffer from a rapid loss of the catalytic activity over time [14].

One of the strategies to improve the performance of existing catalysts is the incorporation of a transition metal (M) element into Pd [14]. Pd−M alloy electrocatalysts have been synthesized by various methods such as co-precipitation, impregnation, sputtering, colloidal methods, and electrodeposition. These have been tested as electrocatalysts in DFAFCs, producing promising results. The synthesis of alloy nanoparticles (NPs), however, themselves remains a paramount challenge. Some methods use high temperatures, which inevitably causes particle aggregation or sintering, thus decreasing the electrocatalytic activity of the catalysts. Other methods require one or more of ancillary additives such as surfactants, reductants, pH adjusters or require multiple steps, thereby raising the production cost [14–23]. A reliable method is required for widespread commercialization.

Recently, sonochemistry has been used in this arena to surmount many of the issues related to the synthesis of NP electrocatalysts because the sonochemical methods have been proven to be efficient for generating NPs and nanoalloys in a short period of time [24–27]. In this study, sonochemistry was used for the synthesis of the NPs of Pd_nM ($n = 1$ for M = Mn, Fe, Co; $n = 1, 2,$ and 3 for M = Ni) supported on carbon (Pd_nM/C) for DFAFC electrocatalysis. The alloy NPs were obtained in one-pot reactions of $Pd(acac)_2$ (acac = acetylacetonate) with an acac-complex of Mn(II), Fe(III), Co(II) or Ni(II). To our best knowledge, PdFe and PdMn NPs have not been reported yet. Our experimental results show that PdM/C catalysts have higher activity and improved durability for FAO than Pd/C.

2. Experimental section

2.1. Chemicals

Palladium(II) acetylacetonate ($Pd(acac)_2$ 99%), nickel(II) acetylacetonate ($Ni(acac)_2$, 95%), cobalt(II) acetylacetonate ($Co(acac)_2$, 97%), iron(III) acetylacetonate ($Fe(acac)_3$, 99.9%), manganese(II) acetylacetonate ($Mn(acac)_2$, 97%), perchloric acid (70%), Palladium black (Pd-black, 99.95%, 40–60 $m^2\ g^{-1}$), and a Nafion solution (5 wt%) were purchased from Aldrich. Ketjen Black (carbon support) was donated from Samsung Advanced Institute of Technology (SAIT). Ethylene glycol (99.9%) and ethanol (99.9%) were purchased from Samchun Pure Chemical Co., and CO gas (99.5%) was purchased from the Deokyang Co. Filter papers were purchased from Whatman. Ultrapure water (Millipore, 18.2 MΩ cm) was used throughout the work.

2.2. Synthesis

$Pd(acac)_2$, a M-reagent, and a carbon support (see details about loading amounts in Table S1) were added into a three-necked flask containing ethylene glycol (30 ml). Pure Ar was bubbled through the solution for 45 min to remove oxygen before the addition of the reagents. A 500 kW ultrasound generator (Sonic and Materials, VC-500, 20 kHz with a 13 mm solid probe) with 30% amplitude was applied for 3 h under an Ar-environment at room temperature. The obtained blackish slurry was filtered, washed with ethanol, and then dried under a vacuum for 12 h at room temperature.

2.3. Characterization

X-ray diffraction (XRD) patterns were recorded with a powder X-ray diffractometer (DC/Max 2000, Rigaku, Cu Kα, $\lambda = 1.54056$ Å). High-resolution transmission electron microscopy (HRTEM) images were obtained on a TEM (JEOL, JE-3011 at 300 kV) to obtain information on the size and size distribution of NPs. Compositions of NPs were obtained by using the energy dispersive X-ray spectroscopy (EDS) apparatus attached to the TEM. High-angle annular dark field (HAADF) images coupled to EDS were recorded on a scanning TEM (STEM, FEI Tecnai G2 F30 at 300 kV) for the elemental distribution of the NPs. A very small amount of the sample was well dispersed by ultrasound in ethanol, and then several drops of the solution were deposited onto a carbon-coated copper grid, followed by drying under ambient conditions. Overall compositions of synthesized samples were obtained by inductively coupled plasma-atomic emission spectroscopy (ICP-AES, OPTIMA 4300DV PerkinElmer). A fixed amount of each sample was dissolved in aqua regia at ∼100 °C for 4 h and then the resulting solution was diluted with distilled water. The carbon support was separated from the solution by using a syringe-filter. Reported compositions are averaged values of three independent measurements on each sample. X-ray photoelectron spectroscopy (XPS, ESCA 2000, VG Microtech.) was conducted with a monochromatic Al Kα source (1486.6 eV) to investigate the electronic and the compositional properties. The reported binding energies (BEs) from XPS are calibrated values with respect to C 1s at 284.8 eV. Fourier-transform infrared spectroscopy (FT-IR, Bruker IFS-66/S) was used to measure the stretching frequencies of CO molecules adsorbed on the electrocatalysts. 5 mg of each sample was ultrasonically dispersed in 10 ml ethanol, and the obtained dispersion was bubbled with CO for 30 min at a blowing speed of 100 cc min^{-1}. The suspended NPs dosed with CO were mounted on KRS-5 (Thallium Bromo-Iodide) for the FT-IR measurement.

2.4. Electrode preparation

5 mg of a sample was dispersed in 2.5 g of distilled water by ultrasound until the dark dispersion became homogeneous. Then, 5 μL of the dispersion was pipetted onto the surface of a glassy carbon rotating disc electrode (RDE, $d = 3.0$ mm, geometric area = 0.0707 cm^2). The catalyst-coated electrode surface was then dried under atmospheric conditions, followed by the addition of 5 μL of a 0.05 wt% Nafion solution on top of the catalyst layer. This Nafion solution was used to mechanically protect the electrode materials.

2.5. Electrochemical measurements

The electrocatalytic activity was evaluated using a potentiostat (Ivium Compactstat, Ivium technology) and a standard three-electrode electrochemical cell equipped with a glassy carbon RDE coated with a catalyst as a working electrode, a Ag/AgCl in KCl (3 M)

reference electrode, and a Pt-net counter electrode for all electrochemical measurements. The working electrode was electrochemically pretreated at the potential range from 0.3 to 1.1 V with a scan rate of 500 mV s^{-1} for 100 cycles before each measurement. Cyclic voltammograms (CVs) were measured in a 0.1 M HClO$_4$ aqueous solution at a scan rate of 50 mV s^{-1} under a N$_2$-environment in the potential range of 0.0–1.25 V. Electrocatalytic activity for FAO was investigated by CV in a 0.1 M HClO$_4$ containing 0.5 M HCOOH at a scan rate of 50 mV s^{-1} in the potential range of 0.0–0.9 V. The stability test was carried out by running cycling tests of 500 cycles in the same conditions as the FAO measurement for all samples. For CO-stripping measurements, a monolayer coating of CO on the electrode was achieved by bubbling CO into the electrolyte for 25 min, while a potential of 0.2 V was applied to the immersed electrode. After purging the solution with N$_2$ for 10 min to remove free CO, CV was performed at a scan rate of 50 mV s^{-1} in the potential range of 0.0–1.25 V.

All electrochemical measurements (CV, FAO, stability test and CO-stripping) were performed at room temperature under ambient pressure, and a fresh electrolyte (0.1 M HClO$_4$) was used for each electrochemical measurement. The reported potentials in this work are corrected with respect to the reversible hydrogen electrode (RHE). Current densities obtained from the CVs, and CO-stripping are normalized with respect to the geometric surface area of an RDE.

3. Results and discussion

3.1. Compositional and structural analyses

Pd$_n$M/C samples were synthesized by sonochemical reactions in ethylene glycol. In each reaction, measured amounts of Pd(acac)$_2$ and a M-reagent were used to make 30 wt% of the metal (Pd + M) content in the final product Pd$_n$M/C in the desired stoichiometric ratio. The compositions analyzed by ICP-AES and EDS agree with each other and show that the reactions are almost quantitative (87–93% based on both Pd and M, Table S1 in the Supplementary content). It must be noted that the reactions have been run without any additives. The solvent ethylene glycol functions as a surface-stabilizer as well as the expected reducing agent. As will be shown below, PdNi/C showed the highest electrocatalytic activity in the PdM/C series. In order to observe the effect of composition on the electrocatalytic activity, we synthesized Pd$_3$Ni/C and Pd$_2$Ni/C following the same procedure. For comparison, we also synthesized Pd/C by the same procedure except that no M-reagent was used.

The XRD patterns of Pd$_n$M/C and Pd/C are shown in Fig. 1. The pattern of Pd/C shows a broad peak at $2\theta = 25.1°$, which is assigned to the (002) plane of the carbon support and a series of peaks at $2\theta = 40°$, 46.5° and 68° which are assigned to the (111), (200), and (220) planes, respectively, of the face-centered cubic (fcc) lattice of Pd (JCPDS no. 87-0643). The patterns of PdM/C samples show similar characteristics, but the peaks are shifted by ~0.5° towards the higher angles from Pd/C. Calculated lattice parameters of PdM/C, $a = 3.865–3.889$ Å, are smaller than that of Pd/C, $a = 3.958$ Å. The lattice parameter of Pd/C is slightly larger than that of pure Pd ($a = 3.918$ Å), which indicates hydrogen absorption in the fcc lattice [28]. Lattice parameters of PdM/C samples are in agreement with data on related materials in the literature such as PdCo (0.388 nm) [28] and (0.386 nm) [29], PdFe (3.89) [30], PdNi (0.3888 nm) [31], and core–shell Co@Pd (0.388 nm) [28]. The decrease in the lattice parameter indicates the incorporation of the M elements into the Pd lattice. The absence of any peak of the M elements or their compounds other than the PdM phases in the XRD patterns suggests that samples are free from macroscopic phase segregation.
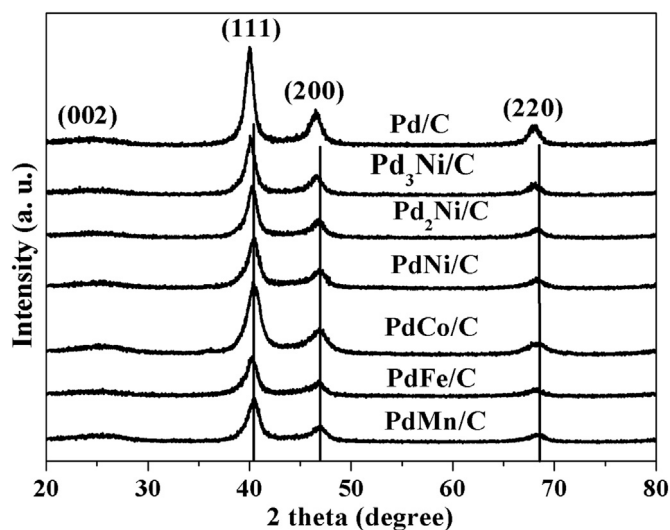

Fig. 1. XRD patterns of Pd/C and Pd$_n$M/C samples ($n = 1$ for M = Mn, Fe, and Co; $n = 1$, 2, and 3 for M = Ni).

Crystallite sizes estimated by the Scherrer equation [32] on the (111) peaks are around 7 nm for all samples (Table 1).

PdM/C samples were analyzed by TEM and EDS for the morphology of the NPs and elemental distribution within individual NPs. We will present the data on PdNi/C here. Data on the other samples are given in the Supplementary content (Figs. S1–3). The low magnification TEM image on PdNi/C in Fig. 2(a) shows that this sample is composed of well dispersed NPs on the carbon support. The particle size distribution histogram in Fig. 2(b), obtained by counting about 100 NPs in the TEM image, shows that the average size is 8.3 ± 1.9 nm, slightly larger than the estimation using the Scherrer equation. As shown, many NPs with triangular shapes are observed, which are probably the (111) facets of the truncated octahedral NPs. Two HRTEM images of two representative PdNi NPs are shown in Fig. 2(c,d). The d-spacings measured from the lattice fringes are at ~0.23 nm, which agree well with $d_{111} = ~0.224$ nm from the XRD pattern. Most of the small (<5 nm) NPs appear to be single crystals, as shown in Fig. 2(c), while the large NPs are polycrystalline, as shown in Fig. 2(d). This explains the larger particle size observed from the TEM image than the crystallite size from the XRD data.

Table 1
Comparison of structural and electrochemical analysis data of Pd/C and Pd$_n$M/C ($n = 1$ for M = Mn, Fe, and Co; $n = 1$, 2, and 3 for M = Ni) electrocatalysts.

Sample	Particle size (nm)[a]	Lattice parameter (Å)[a]	ECSAs from CVs (cm^2)[b]	CO-stripping charge (μC)[c]	Current density (A mg$_{Pd}^{-1}$) at peak potentials (V)[d]	
					Forward	Backward
Pd/C	7.8	3.958	0.875	503.37	0.715 (0.58)	0.601 (0.59)
Pd$_3$Ni/C	7.3	3.889	0.854	408.77	1.516 (0.58)	1.292 (0.58)
Pd$_2$Ni/C	7.2	3.885	0.835	377.39	1.704 (0.55)	1.339 (0.54)
PdNi/C	6.9	3.865	0.804	317.39	2.471 (0.53)	2.094 (0.53)
PdCo/C	7.1	3.866	0.823	326.78	2.330 (0.55)	1.929 (0.56)
PdFe/C	6.8	3.869	0.826	241.6	2.436 (0.58)	1.976 (0.57)
PdMn/C	6.9	3.865	0.769	415.22	2.129 (0.55)	1.834 (0.58)

[a] The crystallite sizes were calculated by Scherrer equation on the (111) peaks of the XRD pattern.
[b] ECSAs calculated from the hydrogen-desorption area of the CVs.
[c] Charge calculated from the anode peaks of the CO-stripping curves.
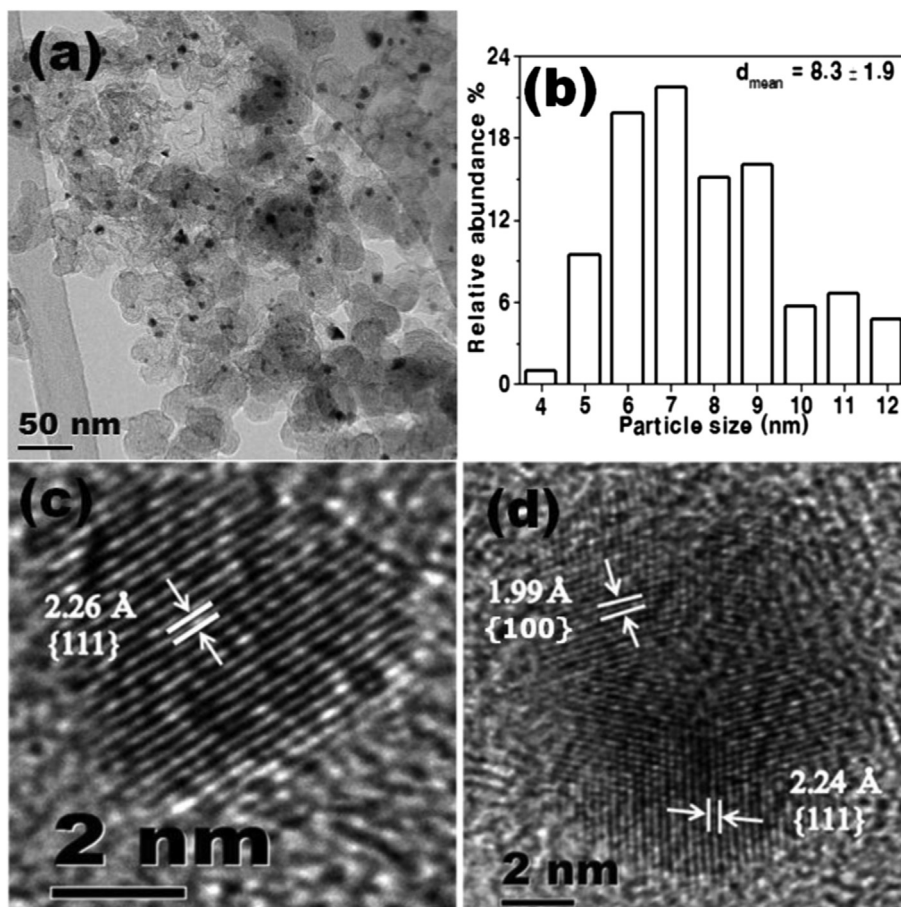[d] Current density from the forward and backward peaks from the CVs of FAO.

Fig. 2. TEM data on PdNi/C: (a) low resolution TEM image, (b) particle size distribution and high resolution TEM images on (c) a small and (d) a large nanoparticle.

Elemental distribution within single NPs was investigated by two different EDS methods, one attached to a conventional TEM (TEM–EDS), and the other attached to an STEM (STEM–EDS). In the TEM–EDS analysis, we selected a few NPs with different shapes and took the EDS spectra at the centers and at the edges. Fig. 3(a,b) shows the results on two different NPs in PdNi/C. The compositions from TEM–EDS (Pd/Ni = 0.95–1.14) agree well with that of the bulk sample by ICP-AES (Pd/Ni = 1.07). Considering that the error range of the EDS elemental analysis is about a few at.%, the two NPs have the same composition both at the center and the edge. These data suggest that the NPs in the sample are uniform in composition and that Pd and Ni are evenly distributed within each of the individual NPs. The latter point is further confirmed by the STEM–EDS line profiles of Pd and Ni within a NP shown in Fig. 3(c). The distribution curves of Pd and Ni show a very close match between them, indicating uniform elemental distribution. Other PdM/C samples are also analyzed in exactly the same way, and their characteristics are analogous to those of PdNi/C (see Supplementary content, Figs. S4–6).

The Pd 3d XPS spectra of Pd/C and PdM/C are shown in Fig. 4(a). The Pd $3d_{5/2}$ and $3d_{3/2}$ peaks of the Pd/C sample appear at 335.59 and
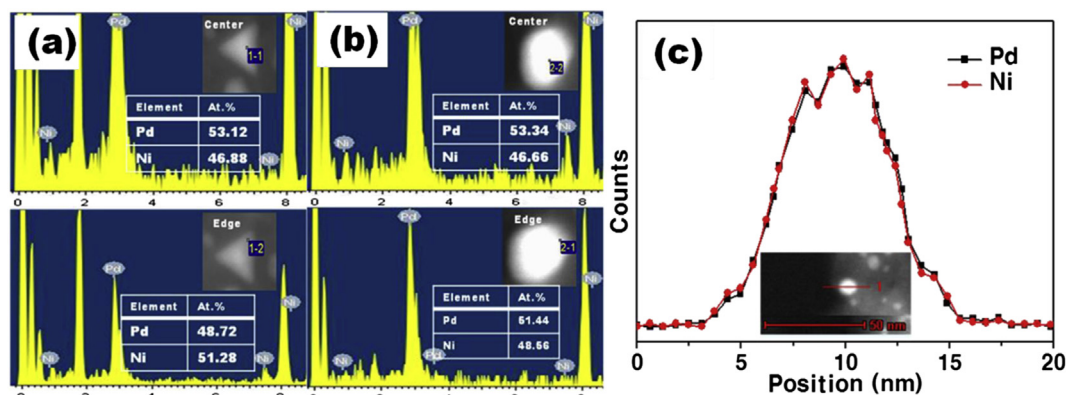

Fig. 3. Elemental distribution analyses on single nanoparticles in PdNi/C: (a) TEM–EDS data on a central and an edge point of a small and (b) a large nanoparticle, and STEM–EDS line profiles for Pd and Ni of a nanoparticle. Inset in (c) is the STEM-HAADF image of the nanoparticle of the STEM–EDS line profile.

340.94 eV, respectively, in good agreement with the values in the literature [32–35]. These peaks are down-shifted in PdM/C samples by 0.4–0.7 eV for both Pd 3d$_{5/2}$ and Pd 3d$_{3/2}$, which can be attributed to the charge transfer from M to Pd atoms. According to the d-band center model by Hammer and Norskov [36], charge-transfer to Pd induces down shift of the Pd d-band center which, in turn, induces weakening of Pd–adsorbate interaction. Kibler et al. [37] and Zhang et al. [38], independently, reported that the down shift of the d-band center of Pd by an appropriate amount increases the electrocatalysis of formic acid on the Pd surface. The magnitude of the XPS peak shifts (ΔBEs) are in the order PdNi ∼ PdMn > PdCo > PdFe. This trend does not follow what one may expect from the trend in the periodic table or the trend of the d-band center theory. Several different factors are likely involved with some having conflicting effects with others. We note that the experimental data on the XPS of Pd in the literature is strongly dependent on the sample state. Surface adsorption of M on Pd films or Pd on M films mostly induces up-shifts of the Pd XPS peaks [39–41]. On the contrary, in most of the data on NPs of Pd with M, the Pd XPS peaks are down-shifted, similar to our data [17,22,32–35]. It seems that the lattice relaxation upon incorporation of M into Pd, which can be fully allowed in the NP systems but not in the bulk or thin film systems, affects the nature and the magnitude of the effect of M to the electronic structure of Pd. XPS spectra show no signature of Pd^{2+} species at around 337.5–337.8 eV for Pd 3d$_{5/2}$ and 342.1–342.6 eV for Pd 3d$_{3/2}$ [42], indicating that our samples are free from surface oxides.

In order to probe the effects of M atoms to the valence electronic state of Pd, the stretching frequencies of CO molecules (ν(CO)) adsorbed on PdM/C and Pd/C (Fig. 4(b)) are studied. The frequency of CO molecules has been used as the measure of the degree of π-back donation of metal d-electrons to π^* orbitals of CO, which reflects the electronic structure of the metal. Because magnetic atoms are strongly unfavorable for interaction with CO [43,44], the ν(CO) data in our PdM NPs are likely on the CO molecules bonded to Pd atoms. Pd/C shows a ν(CO) of 2025 cm^{-1}. This is red-shifted to 1981–1999 cm^{-1} in PdM/C. The magnitude of the peak shift (Δν(CO)) is in the order PdMn > PdCo > PdFe > PdNi. According to the d-band center theory [36], M atoms down-shift the d-band center of Pd with magnitude in the order of M = Mn > Co > Fe > Ni. Because lowering of the d-band level with respect to the Fermi level strengthens the Pd–C π-back donation interaction, the observed trend of ν(CO) can be well accounted for with the d-band center theory.

3.2. Electrochemical studies

Fig. 5(a) shows the CV curves of PdM/C and Pd/C electro-catalysts. All of the faradaic peaks in the CVs are the characteristic features of Pd-containing catalysts. The peaks at ∼0.05 V and ∼0.245 V are assigned to the hydrogen adsorption on the (100) and (111) planes of Pd, respectively [28,45]. The peaks at ∼0.54 V in the anodic sweeps and those at ∼0.7 V in the cathodic sweeps are assigned to the oxide formation and decomposition, respectively. Onset potentials of the oxide formation in PdM/C samples are shifted positively by 26–59 mV from that of Pd/C (inset in Fig. 5(a)), indicating that alloying of Pd with M elements prevents the chemisorption of hydroxyl species, which can be attributed to the down shift of the d-band center of Pd by the M elements. The onset potentials of the oxide formation are in the order of PdNi > PdFe > PdCo > PdMn, which again agrees well with the d-band center theory. Similar effects of alloying have been reported for Pd–M systems [15,46]. Since adsorbed hydroxyl species hinder FAO, the suppression of the hydroxyl group formation on PdM/C is taken as a positive sign for the enhancement in the FAO kinetics through increased active sites. The electrochemical surface areas (ECSAs) of PdM/C samples and Pd/C were calculated from the hydrogen desorption peak intensities of the CVs in Fig. 5(a); the numerical data are listed in Table 1. The electrochemical surface areas of PdM/C are slightly reduced from that of Pd/C. Reduction of ECSAs upon alloy formation may be partly due to the down shift of the Pd d-band center, which weakens binding energy of adatoms.

The cyclic voltammograms of PdM/C samples and Pd/C in a CO saturated electrolyte condition are compared in Fig. 5(b). The peaks of CO-stripping of PdM/C (inset in Fig. 5(b)) are down shifted by 83–57 mV from that of Pd/C, indicating the reduced propensity of CO-poisoning in PdM/C. Magnitudes of peak shifts are in the order PdNi > PdFe > PdCo > PdMn, which agree well with the prediction based on d-band center theory [36]. Integrated peak intensity also must reflect the interaction strength. Peak intensities of PdM are significantly decreased from that of Pd. The trend Pd ≫ PdMn > PdCo > PdNi ≫ PdFe also follows the general trend of the d-band center shift, except that PdFe shows the smallest value instead of lying between PdCo and PdNi. The reason for this deviation from the trend is uncertain. However, we believe that this deviation is related to the magnetism. Through theoretic studies on Pd$_3$Mn (100), Delbeeq and Sautet [47] showed that adsorption of CO on Mn reduces the magnetic moment of Mn, and thus is energetically unfavorable. Fe has the highest magnetic moment among the M atoms studied in the present system. The very strong magnetic moment of Fe likely induces some unpaired spins in Pd which, in turn, affects the bonding with CO. The decreased adsorption strength and affinity to CO of PdM are in general agreement with the literature data [15,16,18,35,38,48]. A reduction in CO binding may result in more active sites for the HCOOH adsorption/desorption and, thus, higher activity for FAO.
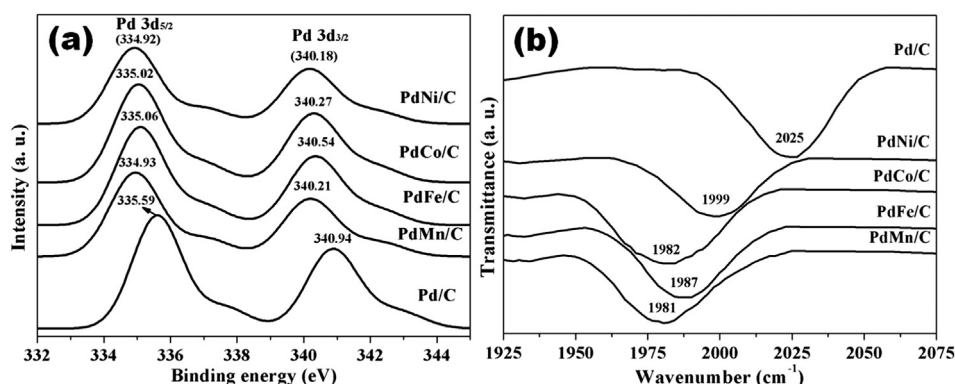

Fig. 4. (a) XPS spectra of Pd/C and PdM/C samples on the Pd 3d region and (b) FT-IR spectra of the CO stretching vibration region on PdM/C and Pd/C samples dosed with CO.
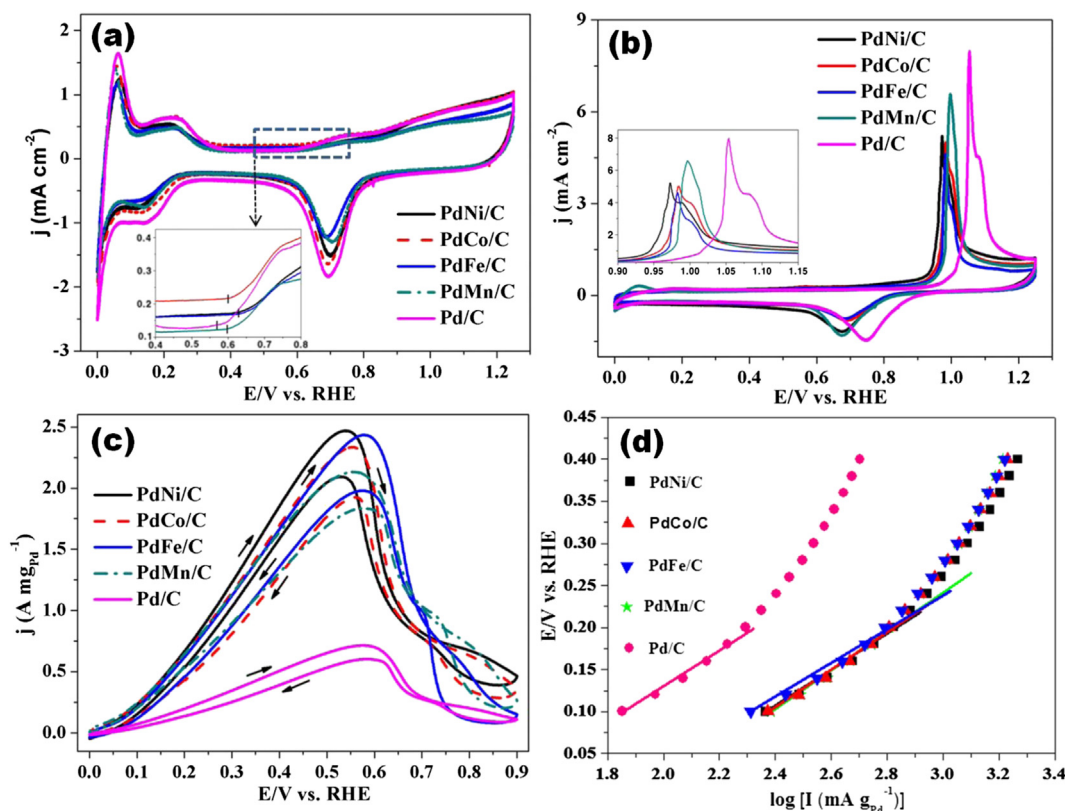
Fig. 5. Electrochemical analysis data on Pd/C and PdM/C samples: (a) CVs (inset is a magnified view of the onset of oxides-formation), (b) CO-stripping (inset is a magnified view of the onset and peak-intensity), (c) CVs of FAO, and (d) Tafel curves for FAO.

The cyclic voltammograms of FAO on PdM/C samples and Pd/C are shown in Fig. 5(c). The numerical data normalized by the Pd masses are summarized in Table 1. As shown in Fig. 5(c), the FAO on all PdM/C samples and Pd/C commences at almost the same potentials, but the reaction kinetics of the FAO on PdM/C are much faster than that of Pd/C. In a typical CV of FAO, the current density in the cathodic scan is reduced from that of the anodic scan, which is due to the presence of residual intermediates hindering the access of the fuel molecules to the electrocatalyst surface. The order of the reactivity toward the FAO among PdM/C samples based on current density at peak potential is PdNi/C > PdFe/C > PdCo/C > PdMn/C, which agrees well with the trend observed in the CO-stripping data and the trend of oxophilicity observed in the CVs. Catalytic activity of PdM/C samples ($1.704–2.471$ A mg_{Pd}^{-1}) is 2–3.5 times higher than Pd/C (0.715 A mg_{Pd}^{-1}). When compared with the FAO activity of Pd-containing catalysts in the literature (~0.370 A mg_{Pd}^{-1} for $Pd_{1.86}Ni_{0.19}$ [16], 0.774 A mg_{Pd}^{-1} for $Pd_{50}Co_{50}$ [14], 0.267 A mg_{Pd}^{-1} for $Pd_{85.5}Co_{13.5}$ [15], 0.5567 A mg_{Pd}^{-1} for $Pd_1Ni_{0.74}$ [35], 0.134 A mg_{PtPd}^{-1} for $Pd_{50}Pt_{30}Ni_{20}$ [31]), our PdM/C catalysts show highly enhanced catalytic activity. We note that two cases of high FAO activity comparable to ours also have been reported. Pt-decorated Pd ($Pd_{20}Pt_1$) [48] is reported to have a peak current density of 2.15 A mg_{Pd}^{-1}. However, the activity of this system is likely due to the majority Pt, not Pd, and direct comparison with our data may not be possible. On the other hand, Li et al. [33] have synthesized a series of Pd–Ni NPs on multi-walled carbon nanotube (MWCNT) supports and found that their PdNi/MWCNT shows a peak current of 2.25 A mg_{Pd}^{-1}, which is much higher than other literature values and comparable to our data. Their data and ours agree in that the electrocatalytic performance can be greatly enhanced if Pd and a TM element are alloyed. However, we also note that the particle size in the work of Li et al. [33] is much smaller (1.6 nm) than ours,

suggesting the high activity in their PdNi/MWCNT may be partly due to the increased surface area.

Since PdNi/C showed the highest activity among the PdM/C series, we tried to locate the optimum composition by comparing the activity of a series of Pd_nNi/C ($n = 1, 2,$ and 3) samples. We found that an increase in the Pd-content does not increase the catalytic activity probably because the amount of charge transfer from Ni decreases as the Pd content increases as evidenced with the XPS data (see Supplementary content, Fig. S7). Li et al. [33] have reported agreeing results that PdNi is superior to Pd_2Ni in FAO. They also showed that $PdNi_2$ had lower activity. Although they do not explain for the latter observation, their data show that the increase of the Ni content higher than PdNi accompanies with the reduction of ECSA, suggesting that too high Ni content decreases the number of catalytically active Pd atoms on the NP surface. The formic acid oxidation kinetics of PdM/C and Pd/C are also compared via Tafel plots, as shown in Fig. 5(d). All of the samples show a linear relationship in the lower output current region. PdM/C samples show higher output current densities and smaller slopes than Pd/C, which agree with the other electrochemical data mentioned above.

In addition to Pd/C, commercial Pd-black was also analyzed for the electrochemical properties to be compared with Pd_nM/C. It turns out that Pd-black is even inferior to Pd/C and, thus, is far inferior to Pd_nM/C (see Supplementary content, Fig. S8). Unfortunately, however, direct comparison with Pd_nM/C electrocatalysts was not possible because the amount of Pd-black required for generating a FAO current density comparable with other samples was at least five-fold excess.

The stability of electrocatalysts in the electrochemical environment is one crucial factor in the application of fuel cells [8,23,33]. Stability of PdM/C samples and Pd/C was tested by running potential sweeps for 500 cycles in an electrolyte of 0.1 M $HClO_4$

containing 0.5 M HCOOH with a scan rate of 50 mV s^{-1} (Fig. 6(a)). The current density decreases slowly with the number of cycles on all PdM/C samples, whereas the current density falls sharply on Pd/C, indicating that PdM NPs have higher stability than Pd. This is probably due to the facilitated removal of intermediates on PdM/C. In order to assess the inherent stability of the electrocatalyst devoid of the effect of a decrease in the concentration of formic acid during the cycling, we ran a potential cycling test on PdNi/C by transferring the electrode into a fresh electrolyte solution after every 100 cycles (inset in Fig. 6(a)). The current density right after each transfer is practically unchanged from the initial value (99.2, 99.5, 99.1, and 98.8% after first, second, third, and fourth 100 cycles, respectively). Therefore, we conclude that the inherent activity of PdNi/C is not decreased during the cycling test.

In order to further verify the durability of the alloy NPs in the present study, the elemental distribution within a NP after the 500 cycling test on PdNi was analyzed by STEM−EDS as shown in Fig. 6(b). The curves of Pd and Ni match well with each other, the same as the plot on a NP before the cycling test in Fig. 3(c), indicating that there is no depletion of Ni or Pd. Therefore, in addition to the result from the cycling test, the elemental distribution data lead to the conclusion that the alloy NPs in the present study are highly durable.
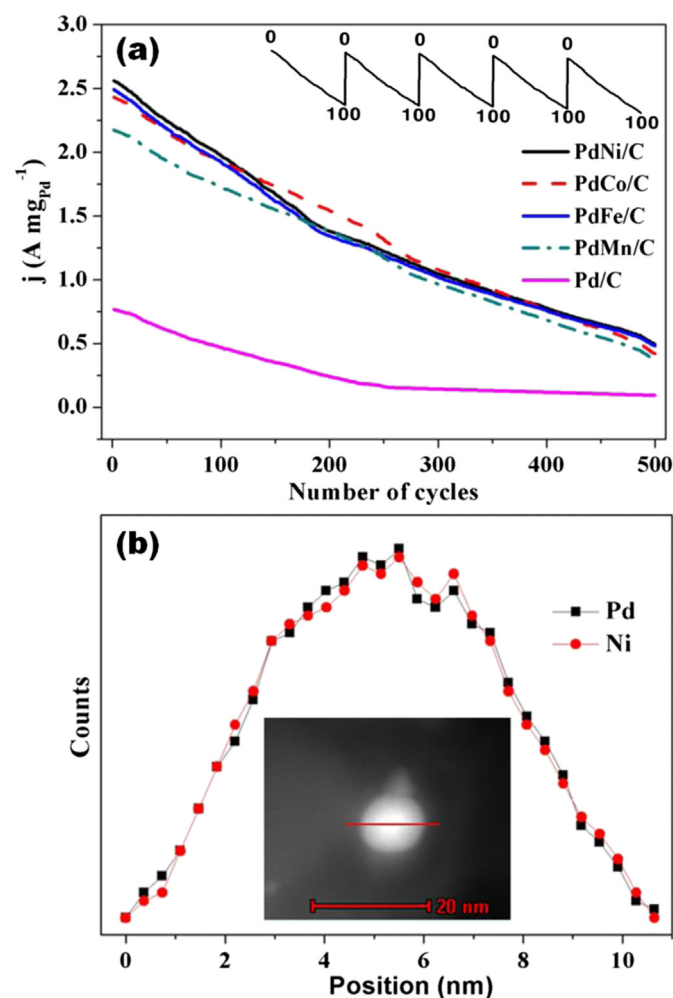

Fig. 6. (a) Stability test results on Pd/C and PdM/C samples. The saw-like curve in the upper part is the result on PdNi/C with the initial electrolyte condition is restored after every 100 cycles. (b) STEM−EDS line profiles for Pd and Ni of a nanoparticle in PdNi/C after running 500 potential cycles between 0.0 and 0.9 V (vs. RHE). Inset in 6(b) is the STEM-HAADF image of the nanoparticle of the STEM−EDS line profile.

4. Conclusion

We report the novel synthesis of bimetallic PdM/C NPs by sonochemical reaction in ethylene glycol. Our synthesis method is a single-step method, not requiring heat-treatment or additives, which are conventionally used in most of the syntheses of alloy NPs. XRD, ICP-AES, TEM, STEM−EDS line profile data, and TEM−EDS data indicate that the NPs are alloys with Pd and the M element uniformly distributed. The XPS and FT-IR data show that the electronic structure of Pd is modified through the interaction with M, which conforms to the d-band center theory. CO-stripping data also confirm this conclusion. The electrocatalytic FAO activity on PdM/C is improved by a factor of 2−3.5 over that of Pd/C. Among the M elements studies, Ni is the most efficient in enhancing the electrocatalytic activity when forming PdM alloys. Furthermore, the Pd/Ni = 1 composition is the optimum for the electrocatalytic performance. Durability is also significantly improved on PdM/C over Pd/C. Therefore, the use of PdM alloy NPs as the FAO electrocatalyst has the advantage not only of reduced cost of materials but also of enhanced activity and durability. In addition, the Ultrasound-assisted polyol synthesis method is a convenient and cost-efficient procedure to produce such PdM NPs, which can contribute to the realization of DFAFCs.

Appendix A. Supplementary data

Supplementary data related to this article can be found at http://dx.doi.org/10.1016/j.jpowsour.2014.03.109.

References

[1] H. Zhao, C. Yu, H. You, S. Yang, Y. Guo, B. Ding, X. Song, J. Mater. Chem. 22 (2012) 4780−4789.
[2] J.M. Feliu, M. Herrero, Handbook of Fuel Cells, Wiley & Sons, Ltd., Chichester, 2003.
[3] S. Zhang, Y. Shao, G. Yin, Y. Lin, Angew. Chem. Int. Ed. 49 (2010) 2211−2214.
[4] M.A. Matin, J.-H. Jang, E. Lee, Y.-U. Kwon, J. Appl. Electrochem. 42 (2012) 827−832.
[5] X. Ji, K.T. Lee, R. Holden, L. Zhang, J. Zhang, G.A. Botton, Nat. Chem. 2 (2010) 286−293.
[6] X. Zhao, J. Zhu, L. Liang, C. Li, C. Liu, W. Xing, Appl. Catal. B: Environ. 129 (2013) 146−152.
[7] S. Uhm, H.J. Lee, Y. Kwon, J. Lee, Angew. Chem. Int. Ed. 47 (2008) 10163−10166.
[8] J. Shim, J. Lee, Y. Ye, J. Hwang, S.-K. Kim, T.-H. Lim, U. Wiesner, J. Lee, ACS Nano 6 (2012) 6870−6881.
[9] T. Ghosh, B.M. Leonard, Q. Zhou, F.J. DiSalvo, Chem. Mater. 22 (2010) 2190−2202.
[10] Y. Lu, W. Chen, Chem. Commun. 47 (2011) 2541−2543.
[11] M. Osawa, K.-I. Komatsu, G. Samjeske, T. Uchida, T. Ikeshoji, A. Cuesta, C. Gutierrez, Angew. Chem. Int. Ed. 50 (2011) 1159−1163.
[12] D. Xu, S. Bliznakov, Z. Liu, J. Fang, N. Dimitrov, Angew. Chem. Int. Ed. 49 (2010) 1282−1285.
[13] S. Zhang, Y. Shao, H.-G. Liao, J. Liu, I.A. Akasay, G. Yin, Y. Lin, Chem. Mater. 23 (2011) 1079−1081.
[14] V. Mazumder, M. Chi, M.N. Mankin, Y. Liu, O. Metin, D. Sun, K.L. More, S. Sun, Nano Lett. 12 (2012) 1102−1106.
[15] L. Zhang, L. Wan, Y. Ma, Y. Chen, Y. Zhou, Y. Tang, T. Lu, Appl. Catal. B: Environ. 138−139 (2013) 229−235.
[16] L. Shen, H. Li, L. Lu, Y. Luo, Y. Tang, Y. Chen, T. Lu, Electrochim. Acta 89 (2013) 497−502.
[17] C. Du, M. Chen, W. Wang, G. Yin, ACS Appl. Mater. Interfaces 3 (2011) 105−109.
[18] L. Dai, S. Zou, J. Power Sources 196 (2011) 9369−9372.
[19] R. Wang, S. Liao, S. Ji, J. Power Sources 180 (2008) 205−208.
[20] Y. Lu, W. Chen, ACS Catal. 2 (2012) 84−90.

[21] H. Wang, Z. Sun, Y. Yang, D. Su, Nanoscale 5 (2013) 139—142.
[22] J. Zhao, A. Sarkar, A. Manthiran, Electrochim. Acta 55 (2010) 1756—1765.
[23] C.V. Rao, B. Viswanathan, Electrochim. Acta 55 (2010) 3002—3007.
[24] Y.T. Didenko, K.S. Suslick, Nature 418 (2002) 394—397.
[25] C. Gumeci, D.U. Cearnaigh, D.J. Casadonte Jr., C. Korzeniewski, J. Mater. Chem. A 1 (2013) 2322—2330.
[26] A. Gedanken, Ultrason. Sonochem. 11 (2004) 47—55.
[27] B.G. Pollet, Int. J. Hydrogen Energy 35 (2010) 11986—12004.
[28] J.-H. Jang, C. Park, Y.-U. Kwon, J. Power Sources 210 (2012) 179—183.
[29] Y. Suo, L. Zhuang, J. Lu, Angew. Chem. Int. Ed. 46 (2007) 2862—2864.
[30] F.I. Pires, H.M. Villullas, Int. J. Hydrogen Energy 37 (2012) 17052—17059.
[31] J. Zhao, K. Jarvis, P. Ferreira, A. Manthiram, J. Power Sources 196 (2011) 4515—4523.
[32] S.Y. Shen, T.S. Zhao, J.B. Xu, Y.S. Li, J. Power Sources 195 (2010) 1001—1006.
[33] R. Li, Z. Wei, T. Huang, A. Yu, Electrochim. Acta 56 (2010) 6860—6865.
[34] L. Chen, H. Guo, T. Fjujita, A. Hirata, W. Zhang, A. Inoue, M. Chen, Adv. Funct. Mater. 21 (2011) 4364—4370.
[35] W. Wang, S. Ji, H. Wang, R. Wang, Fuel Cells 12 (2012) 1129—1133.
[36] B. Hammer, J.K. Norskov, Adv. Catal. 45 (2000) 71—129.
[37] L.A. Kibler, A.M. El-Aziz, R. Hoyer, D.M. Kolb, Angew. Chem. Int. Ed. 44 (2005) 2080—2084.
[38] Z. Zhang, J. Ge, L. Ma, J. Liao, T. Lu, W. Xing, Fuel Cells 9 (2009) 114—120.
[39] J.-H. Choi, T.-U. Nahm, W. Kim, W. Kim, J. Chung, J.-Y. Kim, H. Koh, S.-J. Oh, Surf. Sci. 495 (2001) 173—184.
[40] P. Hermann, J.M. Guigner, B. Tardy, Y. Jugnet, D. Simon, J.-C. Bertolin, J. Catal. 163 (1996) 169—175.
[41] I. Nakamura, H. Hamada, T. Fujitani, Catal. Lett. 87 (2003) 91—96.
[42] X. Guo, P. Brault, G. Zhi, A. Caillard, G. Jin, X. Guo, J. Phys. Chem. C 115 (2011) 24164—24171.
[43] M. Zhou, L. Andrews, J.C.W. Bauschlicher, Chem. Rev. 101 (2001) 1931—1961.
[44] M.P. Felicissimo, O.N. Martyanov, T. Risse, H.-J. Freund, Surf. Sci. 601 (2007) 2105—2116.
[45] M. Jin, H. Zhang, Z. Xie, Y. Xia, Energy Environ. Sci. 5 (2012) 6352—6357.
[46] Y. Pan, F. Zhang, K. Wu, Z. Lu, Y. Chen, Y. Zhou, Y. Tang, T. Lu, Int. J. Hydrogen Energy 37 (2012) 2993—3000.
[47] F. Delbecq, P. Sautet, Chem. Phys. Lett. 302 (1999) 91—97.
[48] X.-M. Wang, M.-E. Wang, D.-D. Zhou, Y.-Y. Xia, Phys. Chem. Chem. Phys. 13 (2011) 13594—13597.